The Seismic Record Supplement to:

Hosgri Fault Transpressional Slip Rates Reproduce Observed Central California Coast Uplift Rates

Daniel O'Connell
Dan.OConnell@tetratech.com
Tetra Tech

Jamey Turner
JTurner@bgcengineering.ca
BGC Engineering

Contents of Supplemental Methods and Data

Introduction

This supplement provides methods and data. Section S1 provides Fig. S1 which reproduces the total magnetic intensity map from PGE (2011). It also includes methods used to estimate uplift rate measurement uncertainties, sensitivity testing to bound reverse slip rate of an onshore reverse-oblique fault (Section S2) as well as the technical approach and basis for input parameters for the viscoelastic deformation modeling of uplift rates (Section S3). It documents the basis for calculating bounds on the maximum reverse slip rate on the onshore San Luis Bay fault zone in Section S43. It documents data set files used to calculate viscoelastic Green's functions, data set input files used to calculate uplift rates for the HFZ north and south fault segments, as well as csv data set spreadsheet files containing measured and calculated uplift rates in Section S5.

The computer codes used to calculate viscoelastic Green's functions are available from https://github.com/pyrocko/fomosto-psgrn-pscmp and can be modified to accommodate large output grids (receivers) and large faults with many source points by modifying Fortran include files to

increase the number receivers and or source points as noted in the README.md displayed in the front page at the web address above.

S1. Total Magnetic Intensity Aeromagnetic Map

Total magnetic intensity data from PGE (2011) are shown in Fig. S1. The Hosgri fault separates lower total magnetic intensity in the Santa Maria Basin on the west side of the Hosgri fault from higher total magnetic intensity regions on the northeast, hangingwall side of the Hosgri fault (Fig. S1). Highest total magnetic intensities between Pt. San Luis and Point Buchon correspond to areas with basalt, diabase, and serpentinite outcrops and shallow subsurface locations of saucer-shaped diabase sills imaged with joint seismic-traveltime-gravity inversion (O'Connell et al., 2015).

S2. Uplift Rate Measurement Uncertainties

Uplift rate measurement uncertainties from measurements of 120 ka (Q2) marine terrace bedrock shoreline angle elevations are required to determine when calculated uplift rates are statistically consistent with uplift rate observations. Hanson et al. (1994) provide estimates of uplift rate uncertainties for a subset of uplift rate measurements. However, Hanson et al. (1994) do not explicitly state what type of uplift rate uncertainties are provided (one-sigma, two-sigma, or some other uncertainty scaling), or if the stated uplift rate uncertainties are meant to account for combined elevation and age data uncertainties or just shoreline angle elevation measurement uncertainties. Also, we need to calculate the uplift rate measurement uncertainties associated with terrace surface shoreline angle elevation measurement uncertainties separately from age-dating uncertainties since the consensus from Hanson et al. (1994) and PG&E (2015) is that 120 ka Q2 terrace surface elevation measurements are most likely from a single age surface even if the age of measured shoreline angle elevations is possibly 100 ka instead of 120 ka. This supplement explains how we use observations from Hanson et al. (1994) and Jefferson et al. (1992) along with photographs of the marine terrace cross sections at sea cliffs in the study area and geophysical observations from a shallow 3D seismic survey (PG&E, 2014) to calculate uplift rate one standard deviation (1σ) measurement uncertainties for all 38 uplift rate measurements that were collected along terraces extending from Pt. San Luis to just north of Islay Creek (Fig. S2).

Marine terrace wavecut bedrock platforms are created during high sea level stands that inundate and erode into bedrock. The eroded wave-cut bedrock surface is then preserved by coastal uplift that raises the bedrock surface high enough to avoid inundation and erosion during subsequent high sea level stands (Fig. S3). The challenge is to map and date marine terrace wave-cut bedrock platform elevations at the highest elevations of the wave-cut bedrock surfaces, denoted by the shoreline angle position in Fig. S3. The shoreline angle is located at the highest inundated elevation of the bedrock surface and is typically buried below surficial deposits of soil and gravel as shown schematically in Fig. S3. The highest resolution measurements of shoreline angle elevations are derived from boring transects of four or more borings positioned to span the shoreline angle position with most of the borings in each boring transect intersecting bedrock near the highest elevations of the bedrock surface to best estimate the shoreline angle elevations.

We first consider the measurement uncertainties of uplift rates primarily estimated using shoreline angle elevations estimated from boring transects. Fig. S4 shows the area between Pt. San Luis and the Diablo Canyon Power Plant (DCPP) with the most boring transects used to estimate shoreline angle elevations that also was the location of a 3D seismic survey. Fig. S5 shows the boring transects in the

same area as Fig. S4 used to constrain the Q2 120 ka shoreline angle elevations in this area between Pt. San Luis and DCPP. Fig. S6 shows a cross section of the marine terrace at the sea cliff location denoted as Figure 2-8 in Fig. S4. As Jefferson et al. (1992) and Hanson et al. (1994) note, the Qm marine lag deposits shown schematically in Fig. S3 are typically 1 m thick between Pt. San Luis and Pt. Buchon but may be locally absent. Thus, short-wavelength roughness and heterogeneity of the eroded bedrock surface introduce measurement noise into estimates of shoreline angle elevations. Hanson et al. (1994) estimate that shoreline angle elevations estimated from boring transects have elevation measurement uncertainties in the range of 0.3-1.0 m primarily due to the roughness of the bedrock surface illustrated in Fig. S6.

Uplift rate measurements between Pt. San Luis and DCPP have the lowest shoreline-angle elevation measurement uncertainties because the elevations were primarily constrained by bedrock depth measurements from 13 boring transects (Fig. S5 shows borings within the extent of the 3D seismic survey). In contrast, there is only one boring transect between DCPP and the last uplift rate measurement north of Islay Creek and shoreline angle elevations are primarily estimated from soil pits or exposures that may have been subjected to erosion. Thus, shoreline elevation measurement uncertainties listed in Hanson et al. (1994) for most sites north of DCPP have shoreline-angle elevation measurement uncertainties three times larger than those estimated for most sites south of DCPP.

The highest shoreline angle elevations, that average about 30 m, primarily occur from DCPP to the last measurement north of the Islay Creek where the shoreline angle elevations uncertainties listed in Hanson et al. (1994) Plate 4 average 2.7 m. Lower shoreline angle elevations ranging from 13 m at Pt. San Luis up to a maximum of 34 m immediately north of DCPP typically have elevation measurement uncertainties of 1 m in Hanson et al. (1994) Plate 4. We convert Hanson et al. (1994) shoreline angle elevations to net uplifts by subtracting a 12-ka paleo sea level of 6 m used by Hanson et al. (1994) for the Q2 120 ka surface. The lowest net uplift uncertainties are in the portion of the profiles from north of Pt. San Luis to DCPP where shoreline angle elevations are 18-34 m yielding one standard-deviation net uplift uncertainties of 4%-8%. The remaining lower shoreline angle elevations in the 12-17 m elevation range between Pt. San Luis and DCPP have one standard-deviation net uplift uncertainties of 9%-17%. Even though the elevation measurement uncertainties are highest north of DCPP the high average shoreline angle elevations in this area yield one standard-deviation measurement uncertainties on net uplift of the Q2 120 ka surface of 11%-13%. For a single-age surface, corresponding uplift rate uncertainties are at least as large as the net uplift rate uncertainties.

These net uplift uncertainties represent a portion of the total net uplift uncertainties. The sea cliff cross section in Fig. S6 shows that the correlation length of bedrock surface roughness is on the order of 2 meters with an average amplitude of 0.5 m (the white hammer is about 0.3 m long in Fig. S6). Borings along individual boring transects are typically about 50 m apart (Fig. S5). The coarse 50 m lateral boring sampling of the rough bedrock surface elevations results in aliased estimates of bedrock surface elevations that introduce long-wavelength biases in estimated shoreline angle elevations.

To quantify measurement uncertainties in estimated shoreline angle elevations derived from the bedrock surface elevations measurements from the coarsely-spaced boring transects in Hanson et al. (1994) we generate correlated- random bedrock surface roughness simulations using a two-dimensional (2D) Von Karman-like self-similar randomization. The Fourier transform of the 2D Von

Karman-like self-similar randomization, with kr being radial wavenumber, a being correlation length, and p=2 is

$$\frac{a^p}{1+(ak_r)^p} \qquad \text{(S1)}$$

When p=3 smoothness increases at shorter wavelengths consistent with the bedrock surface morphology exposed in the sea cliffs (Fig. S6). The average amplitude of the bedrock surface elevation variations is 0.5 m (Fig. S6) with an additional sampling uncertainty of 0.15 m (half a foot since the boring depth data are reported in integer feet). We generate 2D randomizations of the bedrock surface elevation over a 20 km length region, to represent the entire span of the Q2 120 ka marine terrace bedrock surface from Pt. San Luis to just past Islay Creek, at 1 m interval using equation S1 with a=2 m, p=3, and a standard deviation of 0.65 m (midpoint of the elevation uncertainties listed in Hanson et al. (1994) for bedrock elevation estimates from boring transects). We calculate elevation biases of single shoreline angle estimates as the average over four borings per profile position along the profile consistent with the actual sampling sizes of the boring transects used in Hanson et al. (1994) and shown in Fig. S5. There were typically about five borings per profile position estimate of Q2 bedrock elevation in Hanson et al. (1994) but usually at least one boring position was too low or too high to sample the Q2 bedrock surface leaving about four boring locations to estimate shoreline angle elevations at each boring transect.

To approximate a first-order signal from the uplift rate observations, Hanson et al. (1994) recommend setting the uplift rate between DCPP and the last site north of Islay Creek to a single value on the order of 0.02 m/kyr because measurement uncertainties are highest in this region. We follow this recommendation to produce a smooth uplift rate model to fit the observed uplift rate distribute with a constant uplift rate of 0.208 m/kyr from near DCPP to north of Islay Creek and a linear decrease in uplift rate from 0.0208 m/kyr near DCPP to 0.03 m/kyr at Pt San Luis (green circles in Fig. S7). We simulate the process of estimating uplift rates from the smooth model that result from sampling the rough bedrock surface with boring transects using a roughness correlation length (a) of 2 m, and standard deviation of surface roughness of 0.65 m, and p=3 and random phase with the wavenumber spectrum in equation S1. We pick two examples of simulated uplift rate profiles from 200 random phase simulations that illustrate that the observed short-wavelength variability in the measured uplift rates can be reproduced using the simplified uplift rate model (green circles) as a result of course sampling of a rough bedrock surface (Figs. S7 and S8).

Figs. S7 and S8 demonstrate that apparent short-wavelength systematic uplift rate variations can be produced by realistic uncertainties in the measurements of shoreline angle elevations from a moderately irregular bedrock surface. The 1σ randomized uplift rates in Figs. S7 and S8 are 0.014 m/kyr. The standard deviation of the difference of the uplift rate estimates from Hanson et al. (1994) from the smooth (green) uplift rate model is 0.015 m/kyr. Hanson et al. (1994) listed uplift rate uncertainties of 0.02-0.03 m/kyr for measurements between Pt. San Luis and DCPP and 0.03 m/kyr for sites north of DCPP in their Plate 4. Since there are additional factors, like paleo sea stacks (Fig. S4) that locally increase bedrock surface elevations variability, the uplift rate uncertainties of Hanson et al. (1994) provide reasonable estimates of 1σ uplift rate measurement uncertainties. The Hanson et al. (1994) uplift rate measurement uncertainties of 0.03 m/kyr for the uplift rate measurements between Pt. San Luis and DCPP in their Plate 4 seem pessimistic. More recent seismic measurements of the long-wavelength Q2 120 ka bedrock surface elevation (PG&E, 2014) suggest that shoreline angle elevation measurement uncertainties of 1 m in Hanson et al.'s (1994) Plate 4 are realistic; then

corresponding 1σ uplift rate uncertainties due to elevation measurement uncertainties are 0.02 m/kyr for the uplift rates estimates from Pt. San Luis to just north of DCPP.

To compare calculated uplift rates to measured uplift rates we assign 1σ uplift rate uncertainties of 0.02 m/kyr for the uplift rate estimates of Hanson et al (1994) that extend from Pt. San Luis to about one km north of DCPP (profile distances of 0-11.2 km in Figs. S7 and S8). We assign 1σ uplift rate uncertainties of 0.03 m/kyr for the nine northernmost uplift rate estimates north of DCPP to account for the ~50% larger net uplift measurement uncertainties at these sites due to the lack of boring profiles. Then, we can use uplift rate misfit to determine when HFZ deformation models of uplift rates are consistent with measured uplift rates within measurement uncertainties and use uplift rate misfit to find the largest reverse-slip rate that can be assigned to an additional fault intersected the uplift rate profile and still produce uplift rates consistent with the observed uplift rate as illustrated in the Section S4.

S3. Viscoelastic Deformation Modeling of Uplift Rates

Previous kinematic analyses for the Irish Hills, summarized in PG&E (2015), used rigid block models with onshore thrust-reverse faults and variations in the bounding fault geometries and slip rates to explain observed uplift rates in the Irish Hills. For example Lettis and Hall (1994) interpreted the San Luis Bay/Pismo structural block to be actively uplifting by slip on northwest-trending oblique and pure dip-slip faults. Work published in PG&E (2011) interprets the Irish Hills range to be a rigid crustal block somewhat uniformly uplifting by thrust-reverse motion on the onshore bordering Los Osos and Southwest Boundary zone faults. However, high resolution seafloor bathymetric data reveals exposed Neogene bedrock on the seafloor shelf to the southwest of the Irish Hills, and sea-floor and seismic reflection fault mapping indicates that older contractional out-of-syncline fold and thrust structures, that developed during inversion of the Pismo Basin, are cut and offset by younger, linear, vertical to sub-vertical strike-slip faults that are not folded (Fig. S9). This suggests the strike slip faults either postdate folding and thrusting, or the thrust-reverse faulting slip rates are much lower than the strike-slip faulting slip rates (Angell, et al., 2015).

In contrast to rigid block models, we use published constraints on HFZ slip rates and geometry (Hanson et al., 2004; Johnson & Watt; 2012; PG&E, 2015) with a linear Green's function viscoelastic crustal-upper mantle deformation modeling approach (Wang et al., 2006) to calculate offshore and onshore uplift rates associated with long-term HFZ earthquake deformation. For this study area, a linear viscoelastic Green's function approach is adequate to calculate uplift rates because the sum of total slips that occur over 120 kyr on these HFZ segments are partitioned to < 0.2 km of horizontal slip and < 0.075 km of reverse slip using published mean slip rates (Hanson et al., 2004; Johnson & Watt, 2012). Consequently, the total fault deformations are sufficiently small that the crustal-scale HFZ geometry is unchanged to first order over 120 kyr, allowing linear viscoelastic Green's functions to adequately represent long-term uplift rate responses. A linear Green's function approach is not adequate to model nonlinear extensional deformation within the ~12 km-long releasing right-step region in the HFZ over 120 kyr because differential right-slip in the HFZ step-over produces 0.36 km of extension, corresponding to a finite extensional strain of 3%. We use the linear viscoelastic Green's function approach to model uplift rates that are controlled by the reverse-component of slip rates. Sensitivity testing showed that modeled uplift rates in the Irish Hills are insensitive to horizontal slip rates to first order.

Wang et al. (2006) calculate viscoelastic Green's functions with an orthonormalization technique to avoid loss of precision and an anti-aliasing extension to the Fourier transform that ensures numerical stability when calculating post-seismic deformation over time. Wang et al. (2006) model post-seismic responses to the 1960 **M** 9.5 great Valdivia, Chile, subduction earthquake to calculate the changes in vertical displacement over time due to afterslip and viscoelastic responses of the crust and mantle. Wang et al. (2006) show that post-earthquake vertical deformation rates extend over several hundred years before vanishing. These types of viscoelastic post-earthquake deformation calculations are also typically used with GPS measurements of post-earthquake deformations over years to decades to estimate viscosities for the lower crustal and mantle (Bürgmann & Dresen, 2008; Thatcher & Pollitz, 2008). Here we use published constraints on crustal-mantle viscoelastic structure (as discussed below) to calculate post-earthquake deformation over time like Wang et al. (2006), until post-seismic deformation rates approach zero, to allow complete viscoelastic relaxation, and thus calculate long-term uplift rates associated with repeated HFZ earthquake cycles over 120 kyr.

A one-dimensional (1D) crustal–mantle viscoelastic model (supplemental Data Set S1) was constructed using a lateral average of 3D P-wave tomography models for the shallow crust (Zhou et al., 2014) and a lateral average of the mid- and lower-crustal 3D P- and S-wave model from Hardebeck (2010). The crustal velocity model includes the following parameterizations: a 0.5 km-thick standard-linear-solid layer with a transient viscosity of 10^{18} Pa-s to represent shallow Quaternary sedimentary rocks in the HFZ; from 0.5–15 km depth the crust is elastic (Howie et al., 1993; Miller et al., 1992); from 15–25 km, the likely mostly mafic lower crust (Howie et al., 1993; Miller et al., 1992) is assigned a standard-linear-solid with a transient viscosity of 10^{20} Pa-s; below 25 km the upper mantle is assigned a Maxwell body steady-state viscosity of 10^{19} Pa-s. These lower crustal and mantle viscosities are typical of actively deforming regions in the western United States from Thatcher and Pollitz (2008). These viscosities are slightly higher than viscosities used by Pollitz and Thatcher (2010) to model Hector Mine post-earthquake deformation east of the SAF. This 1D viscoelastic crustal and upper-mantle velocity-density-viscosity model required calculating deformation out to > 500 years post-earthquake to reach equilibrium (vanishing post-seismic uplift rates). Thus, viscoelastic deformations were calculated to 511 years during modeling of uplift rates. Because 511 years is much shorter than earthquake recurrence times on the HFZ and adjacent faults (PG&E, 2015), calculated viscoelastic uplift rates after 511 years represent long-term uplift rates.

Long-term uplift rate constraints are used in our modeling because historical uplift rate data are strongly influenced by interseismic transient deformation of the San Andreas fault (SAF) and related fault system (Howell et al., 2016; Smith-Konter et al., 2014). Post-1857 SAF earthquake uplift observed along this portion of the central California coast are likely dominated by interseismic uplift caused by bending moments applied at the ends of the locked SAF 1857-earthquake segment (Smith-Konter et al., 2014). Deformation analyses of the SAF and other major California fault systems (Howell et al., 2016) suggest that SAF system interseismic deformation produces historical uplift rates along the coast near the HFZ that can be 2-3 times higher than the 0.20-0.25 m/kyr maximum observed uplift rates of the Q2 (~120 ka) emergent marine terrace. Thus, along the Irish Hills portion of CCC, the post-Q2 (~120 ka) long-term marine terrace uplift rate constraints from Hanson et al. (1994) presented in Section S1 provide a valuable data set that average over many complete earthquake cycles, and thus isolate long-term uplift rates.

Dextral slip rates are included to ensure an appropriate radiation pattern is imposed in the deformation calculations consistent with geologic estimates of dextral slip rates. A simplified dextral slip rate model with 1.7 m/kyr dextral slip rate on the north HFZ segment and to 1.35 m/kyr on the

south HFZ segment, consistent with Hanson et al. (2004), is used in the final slip rate model. This is consistent with observations that suggest the HFZ dextral slip rates decrease from north to south across the HFZ step-over (Hanson et al., 2004; Johnson and Watt, 2012).

Fault slip rates are only varied along strike with constant slip rates assigned to the 15 km-depth extent of the fault in the elastic crust. Dip slip rates and fault dips are varied as little as possible along strike (Figure 5a) to find fault parameters with the least complexity that matched observed marine terrace uplift rates. The forward modeling started with a uniform dip-slip rate of 0.45 m/kyr which is between the average HFZ vertical slip rates of Hanson et al. (2004) and Johnson and Watt (2012) to create a simple starting model that reproduced uplift rates broadly consistent with the observed uplift rate data. Constraints on HFZ dip from PG&E (2015) were used to limit fault dips to vary between 75°-85° with dips along most of the HFZ set to 80° (Figure S12a). Dip-slip rates and dips were adjusted as little as possible within the data constraints from Hanson et al. (2004), Johnson and Watt (2012), and PG&E (2015) to find a HFZ dip-slip rate model that reproduced observed uplift rates along the marine terraces within uplift rate measurement uncertainties of 0.02-0.03 m/kyr . Supplemental Data Set S2 contains the input for calculating north HFZ segment contributions to uplift rates. Supplemental Data Set S3 contains the input for calculating south HFZ segment contributions to uplift rates which must be multiplied by 0.75, summed with uplift rates produced by the north HFZ segment, and increased by 0.01 m/kyr (to account for regional uplift) to reproduce the uplift results of this paper are provided in supplemental Data Sets S4 and S5.

S4. Bounds on Maximum Reverse Slip Rate on the San Luis Bay Fault Zone

The San Luis Bay (SLB) fault zone is a postulated steeply-north-dipping reverse-oblique fault that crossing the uplift rate profile region east of the HFZ between Pt. San Luis and DCPP (Fig. S10). We model the SLB fault zone as a single fault dipping north at 80° with a dextral slip rate of 0.1 m/kyr and progressively increase the SLB fault zone reverse-slip rate until the misfit between calculated total uplift rates from the combined HFZ and SLB fault zone deformation and the measured uplift rates exceeds the expected misfit.

A reverse slip rate of 0.04 m/kyr on the SLB fault produces four exceedences of the 2σ uplift rate measurement uncertainties which is more than twice the expected misfit rate of two exceedences at 2σ (Fig. S11). Consequently, the maximum reverse-slip rate for the SLB fault is bounded to be < 0.04 m/kyr based on the current uplift rate data.

S5. Data Set Files

Input files are provided for the two programs that were used to calculate viscoelastic Green's functions and free-surface deformations. These two programs described in Wang et al. (2006) include psgrn08 to calculate viscoelastic Green's function and pscmp08a to calculate free-surface deformations. Fig. S1 shows the entire map area extent of the Hosgri fault segments as red lines that were used in the deformation calculations. The input file containing the information required to calculate the 1D viscoelastic Green's functions using psgrn08 is provided in Data Set S1. The pscmp08a input files containing the geographic coordinates and geometries of the two fault segments are provided in Data Set S2 for the north Hosgri segment and Data Set S3 for the south Hosgri segment. Source and executables for the software documented in Wang et al. (2006) where obtained from https://gitext.gfz-potsdam.de/fomosto-backends/fomosto-psgrn-pscmp. The pscmp08a source

code was modified to increase variable dimensions enough to output higher resolution geographic output of deformation parameters contained in the uplift grid output file in Data Set S4.

Data Set S5 contains the measured uplift rate data from Hanson et al. (1994) and the corresponding calculated uplift rates. Estimates of measured uplift rate measurement uncertainties associated with measurement uncertainties of the elevations of the bedrock surfaces buried beneath soil listed in Data Set S5 are documented in Section S2 of this supplement.

Data Set S1. Input file for the program "psgrn08" to calculate viscoelastic Green's function. This file contains the crustal-mantle viscoelastic model used to calculate Green's functions at the bottom of the file.

Data Set S2. Input file for the program "pscmp08" to calculate north Hosgri fault contributions to post-seismic deformation.

Data Set S3. Input file for the program "pscmp08" to calculate south Hosgri fault contributions to post-seismic deformation. Uplift rates should be scaled by 0.75, summed with uplift rates from the output from Data Set S2, and multiplied by -1 to obtain total uplift rates presented in the paper and contained in Data Set S4.

Data Set S4. Output spreadsheet file with calculated total uplift rates from the final north and south Hosgri fault segment models (data sets S2 and S3) as a function of decimal latitude and longitude.

Data Set S5. Output spreadsheet file with locations of measured marine terrace uplift rates in decimal latitude and longitude as well as profile distance in km from the first location near Point San Luis as plotted in Figure 4B along with measured and calculated uplift rates in m/kyr.

Supplementary References

Angell, M., M. Buga, J. Turner, J. Sowers, and S. Nishenko (2015). Revised Offshore Mapping of Fault and Fold Deformation Associated with the Hosgri Fault Zone, the Point Buchon Fault and the Shoreline Fault, Central Coastal California, *Seism. Res. Lett.* **86**, 79-80.

R. Bürgmann and G. Dresen (2008). Rheology of the Lower Crust and Upper Mantle: Evidence from Rock Mechanics, Geodesy, and Field Observations, *Ann. Rev. Earth & Planet. Sci.* **36**, (1), 531-567. DOI: 10.1146/annurev.earth.36.031207.124326.

Hanson, K.L., J.R. Wesling, W.R. Lettis, K.I. Kelson, and L. Mezger (1994). Correlation, ages, and uplift rates of Quaternary marine terraces, south-central California, in *Seismotectonics of the Central California Coast Range*, Alterman, I.B., McMullen, R.B., Cluff, L.S., and Slemmons, D.B. (Editors), *Geol. Soc. Am. Spec. Pap.* 292, 45–72.

Hardebeck, J.L. (2010). Seismotectonics and fault structure of the California central coast, *Bull. Seismol. Soc. Am* **100**, 1031–1050, doi: 10.1785/0120090307.

Howell, S., B. Smith-Konter, N. Frazer, X. Tong, D., and D. Sandwell (2016). The vertical fingerprint of earthquake cycle loading in southern California, *Nature Geoscience* **9**, 611–614. doi:10.1038/ngeo2741.

Howie, J.M., K.C. Miller, and W.U. Savage (1993). Integrated crustal structure across the south central California margin: Santa Lucia Escarpment to the San Andreas fault, *J. Geophys. Res.* **98**, 8173-8196.

Jefferson, G. T., H. L. Fierstine, J. R. Wesling, and T.-L. Ku (1992). Pleistocene terrestrial vertebrates from near Point San Luis, and other localities in San Luis Obispo County, California, *Bull. Southern California Acad. Sci.* **9** (11), 26-38.

Johnson, S.Y. and J.T. Watt (2012). Influence of fault trend, bends, and convergence on shallow structure and geomorphology of the Hosgri strike-slip fault, offshore central California, *Geosphere* **8**, 1632-1656.

Lettis, W.R., and N.T. Hall (1994), Los Osos fault zone, San Luis Obispo County, California: in *Seismotectonics of the Central California Coast Ranges*, Alterman, I.B., McMullen, R.B., Cluff, L.S., and Slemmons, D.B. (Dditors), *Geol. Soc. Am. Special Paper 292*, 73–102.

Lettis, W.R., K.L. Hanson, J.R. Unruh, M. McLaren and W.U. Savage (2004). Quaternary tectonic setting of south-central coastal California, in *Evolution of Sedimentary Basins/Offshore Oil and Gas Investigations—Santa Maria Province*, Keller, M.A., (Editor), *U.S. Geol. Surv. Bull. 1995-AA*, 24 pp.

Miller, K.C., J.M. Howie, and S.D. Ruppert (1992). Shortening within underplated oceanic crust beneath the central California margin, *J. Geophys. Res.* **97** (B13), 19961-19980.

O'Connell, D.R.H., J. P. Turner, J. Goodman, L. Lajoie, J. Sowers, M. Angell, S. Nishenko, D. Zhou, and W. Wang (2015). 3D Subsurface Structural Imaging of the Irish Hills, California, Using Active Seismic, Gravity, and Magnetic Data, *Seis Res. Lett.* **86**, 699.

Pacific Gas and Electric Company (PG&E) (2011). Report on the Analysis of the Shoreline Fault Zone, Central Coastal California, report to the U.S. Nuc. Reg. Comm., January.

Pacific Gas and Electric Company (PG&E) (2014). Chapter 8: 2012 3D Onshore Seismic Survey: in *Central Coastal California Seismic Imaging Project,* report to the California Public Utilities Commission; available https://www.pge.com/en_US/safety/how-the-system-works/diablo-canyon-power-plant/seismic-safety-at-diablo-canyon/seismic-report.page.

Pacific Gas and Electric Company (PG&E) (2015). Seismic Source Characterization for the Diablo Canyon Power Plant, San Luis Obispo County, California; report on the results of a SSHAC level 3 study, Rev. A, March 2015. Available online at http://www.lettisci.com/sshac3/DCPP_SSC_Report_Rev_A.zip (last accessed 22 November 2022).

Pollitz, F.F. (1986), Pliocene change in Pacific-plate motion, *Nature* **320**, 738- 741.

Pollitz, F., and W. Thatcher (2010). On the resolution of shallow mantle viscosity structure using post-earthquake relaxation data: Application to the 1999 Hector Mine, California, earthquake, *Geophys. J. Int.* **115**, Q06008, doi:10.1029/2010JB007405.

Smith-Konter, B.R., G. M. Thornton, and D.T. Sandwell (2014). Vertical crustal displacement due to interseismic deformation along the San Andreas fault: Constraints from tide gauges, *Geophys. Res. Lett.* **41** (11), 3793–3801. doi: 10.1002/2014GL060091.

Thatcher W, and F.F. Pollitz (2008). Temporal evolution of continental lithospheric strength in actively deforming regions, *GSA Today* **18**, 4–11.

Wang, R., F. Lorenzo-Martin, and F. Roth (2006). PSGRN/PSCMP – a new code for calculating co- and post-seismic deformation, geoid and gravity changes based on the viscoelastic-gravitational dislocation theory, *Computers & Geosciences* **32**, 527–541.

Supplementary Figures S1-S11

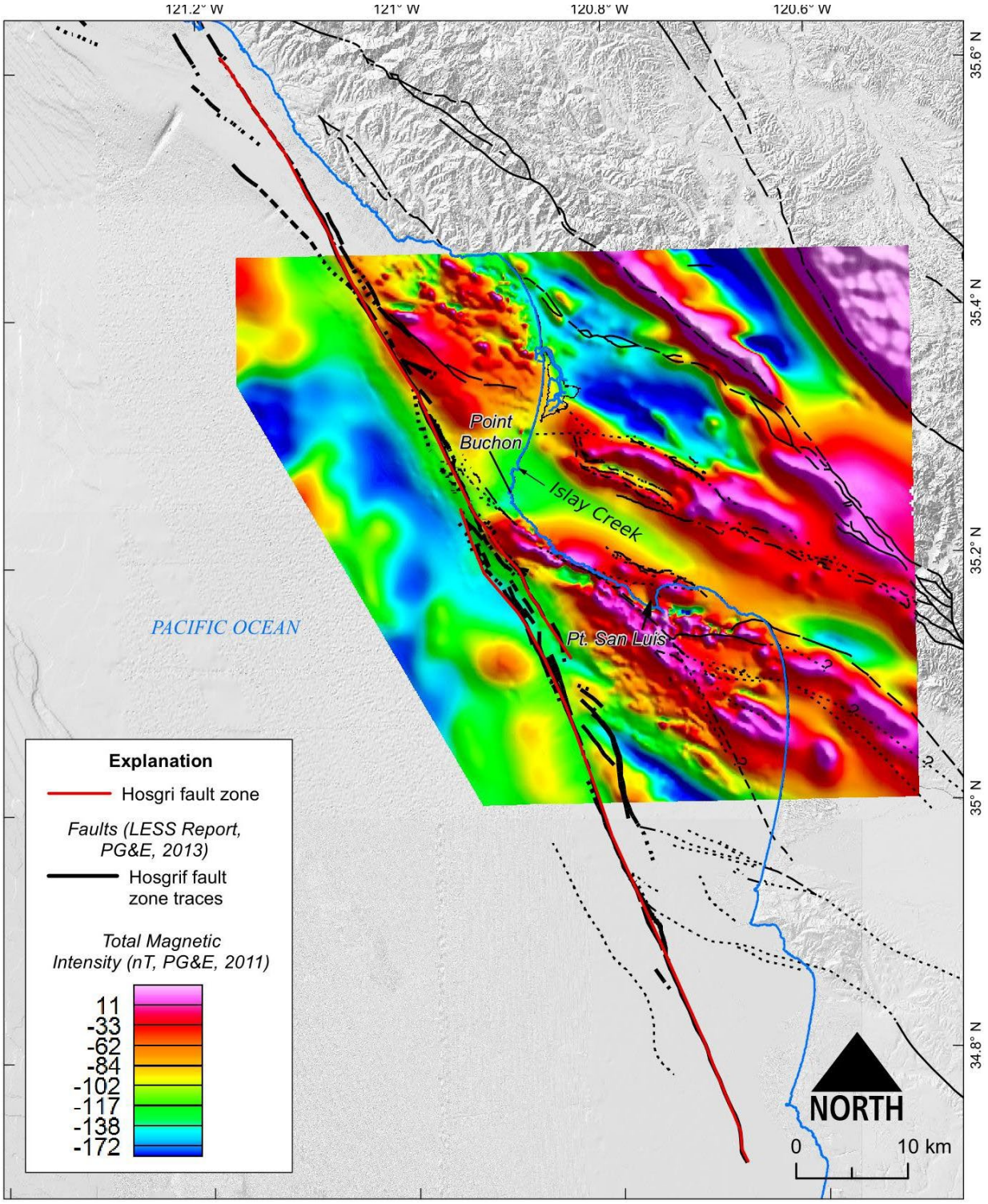

Figure S1. Hosgri fault zone and other faults as thinner lines with aeromagnetic map. Regional faults (thin black solid, dotted, and dashed lines), Hosgri fault zone traces (thick black solid, dotted, and dashed lines) and color-coded aeromagnetic total magnetic intensity map superimposed on gray-shaded topography. The coastline is the blue line.

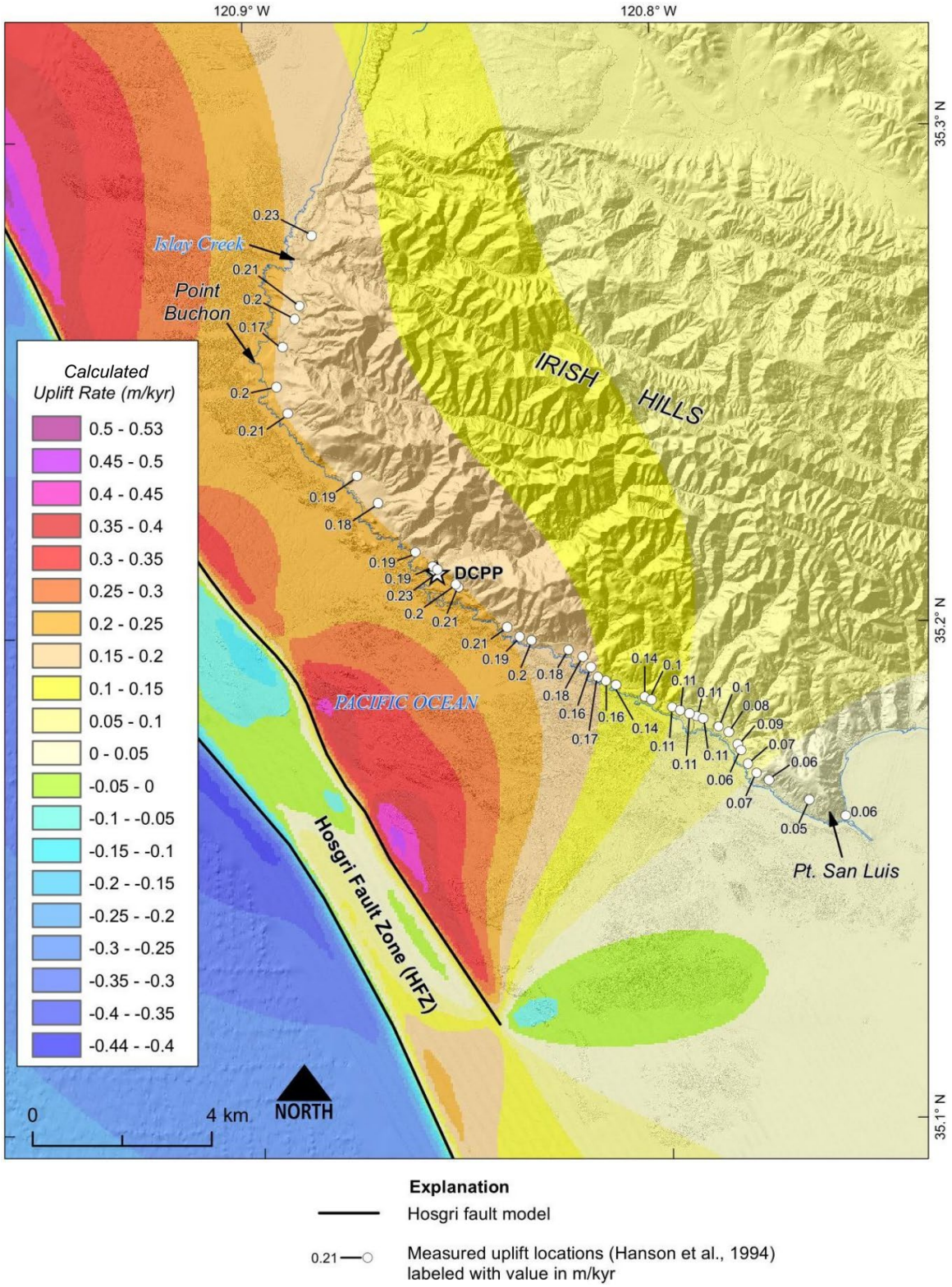

Figure S2. Uplift rate measurement locations and values with calculated uplift rate color map. Uplift rate measurement locations are shown as white circles labeled by measured uplift rate in m/kyr. Color contours show calculated uplift rates for the final HFZ uplift rate model.

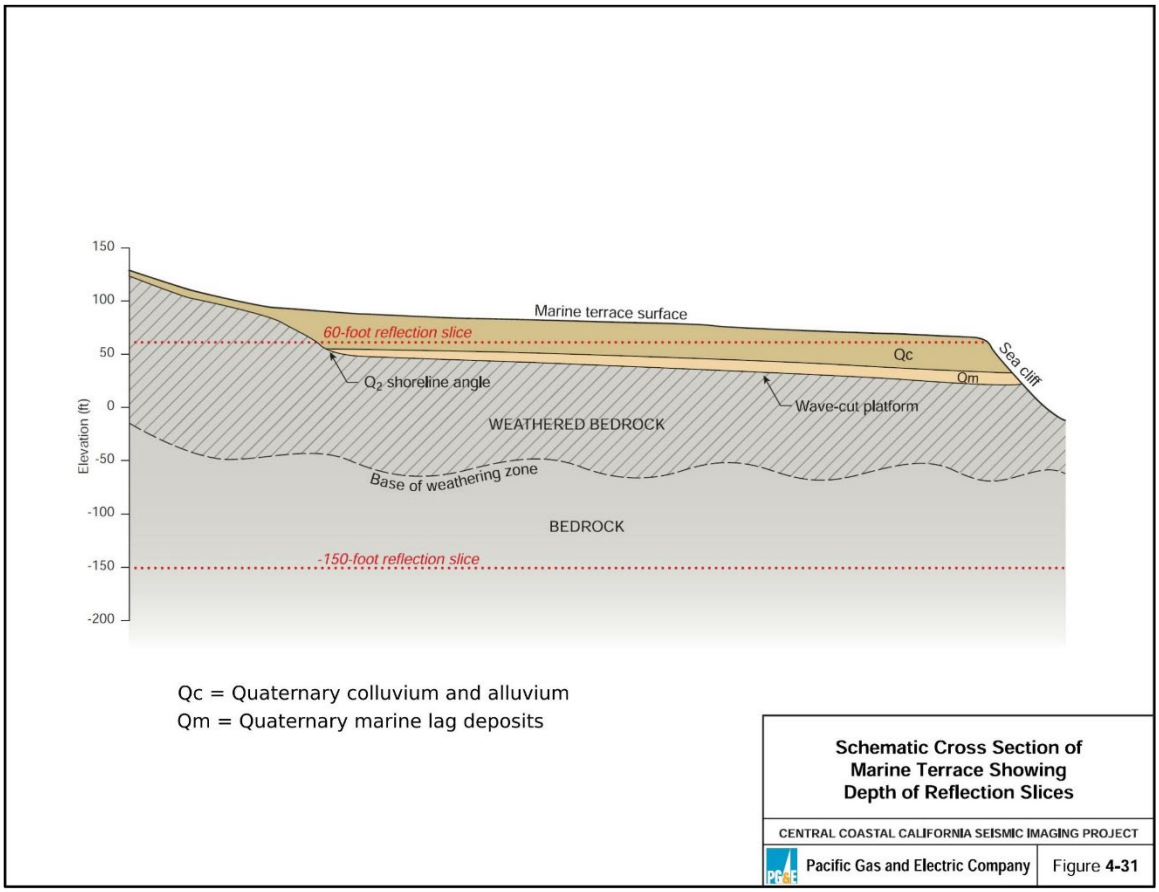

Figure S3. Map Schematic cross section of a marine terrace showing location of shoreline angle elevations and the depth range of 3D seismic reflection and tomographic imaging below the marine terrace surface.

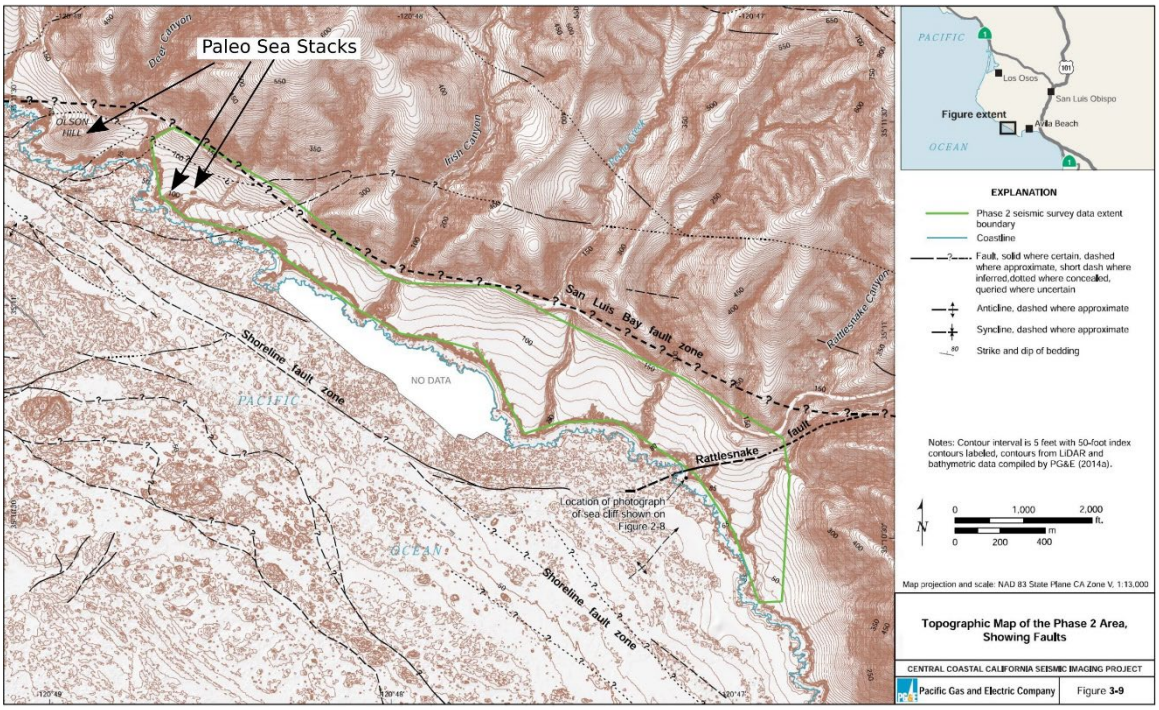

Figure S4. Map showing the topography of the marine terrace in the area encompassed by the PG&E (2014b) 3D seismic reflection and tomography survey (areas outlined in green is the 3D seismic survey area). The location of the photograph in Figure S6 is labeled “Location of photograph of sea cliff shown in Figure 2-8”. The onshore high-resolution 3D seismic data acquired in 2012 within the green polygon showed that sub-soil marine terrace bedrock elevations are consistent with boring data used in Hanson et al. (1994) and not vertically offset by faults within the green polygon area (PG&E, 2014).

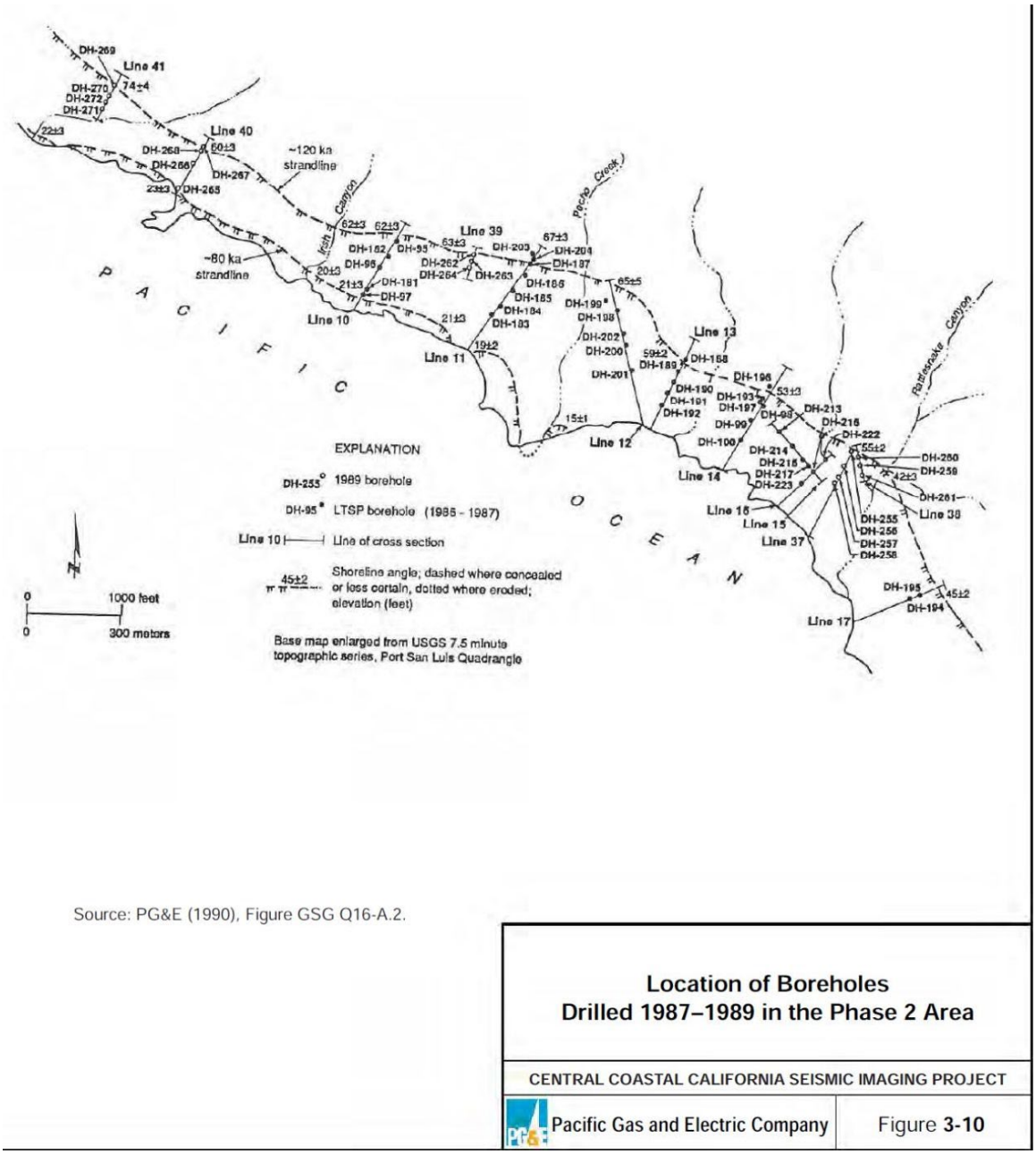

Figure S5. Location of boreholes used in Hanson et al. (1994) to estimate elevations of the 120 ka marine terrace shoreline angles in the area encompassed by the 3D seismic reflection and tomography survey of PG&E (2014).

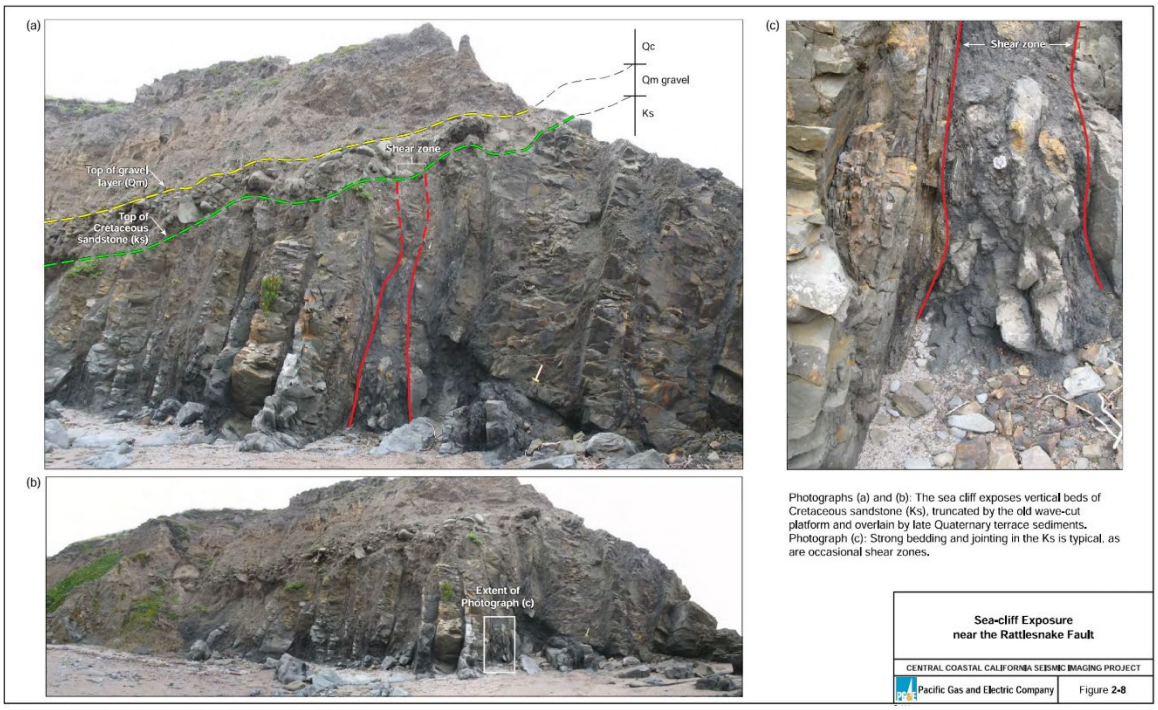

Qc = Quaternary colluvium and alluvium
Qm = Quaternary marine lag deposits

Figure S6. Sea cliff exposure of a cross section of the marine terrace. Cliff photographs show the exposed marine terrace cross section at the location indicated in Figure S4 as Figure 2-8.

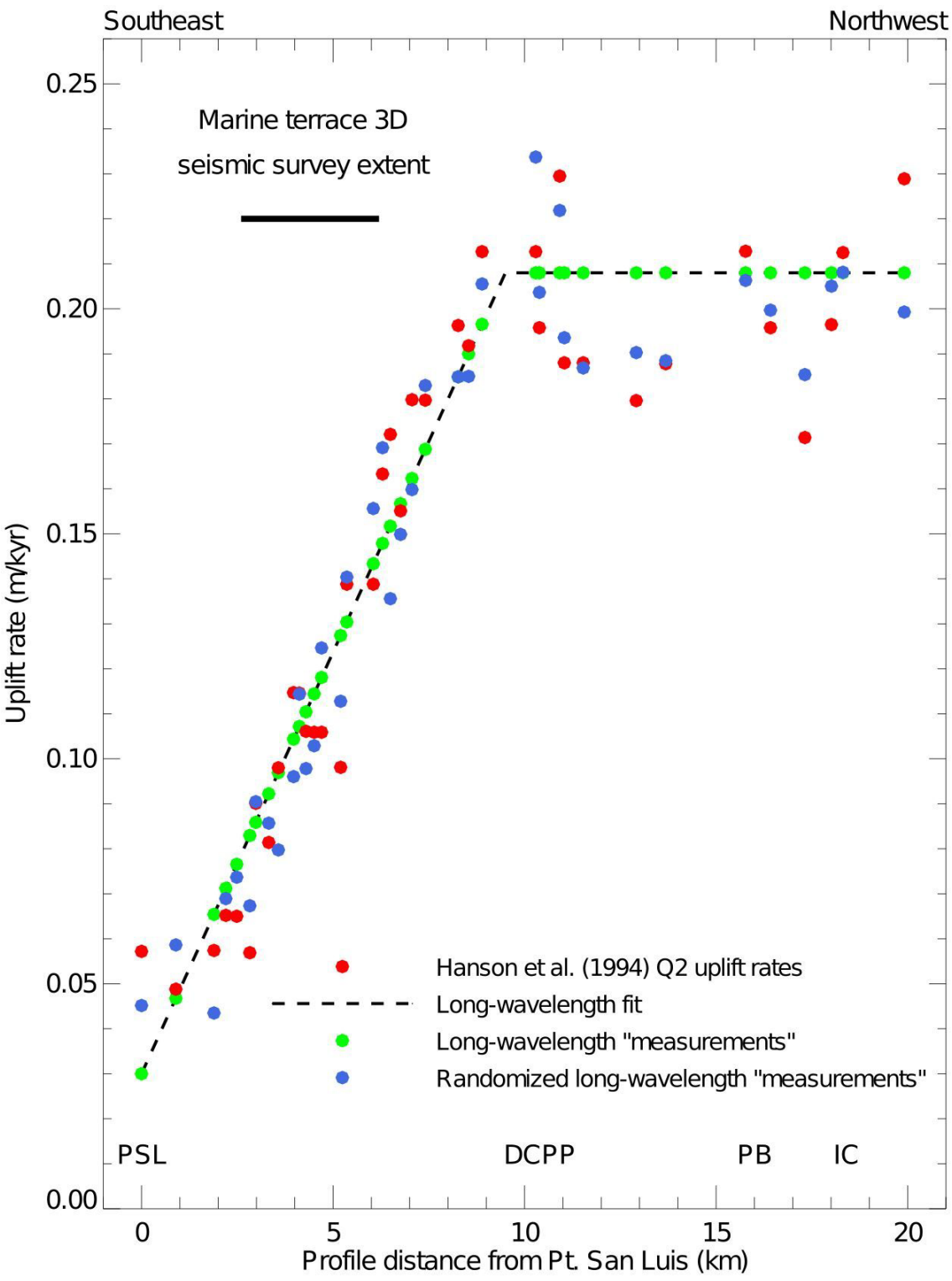

Figure S7. Simulation 1 of Hanson et al. (1994) uplift rate data with red circles as the measured uplift rates from Hanson et al. (1994).

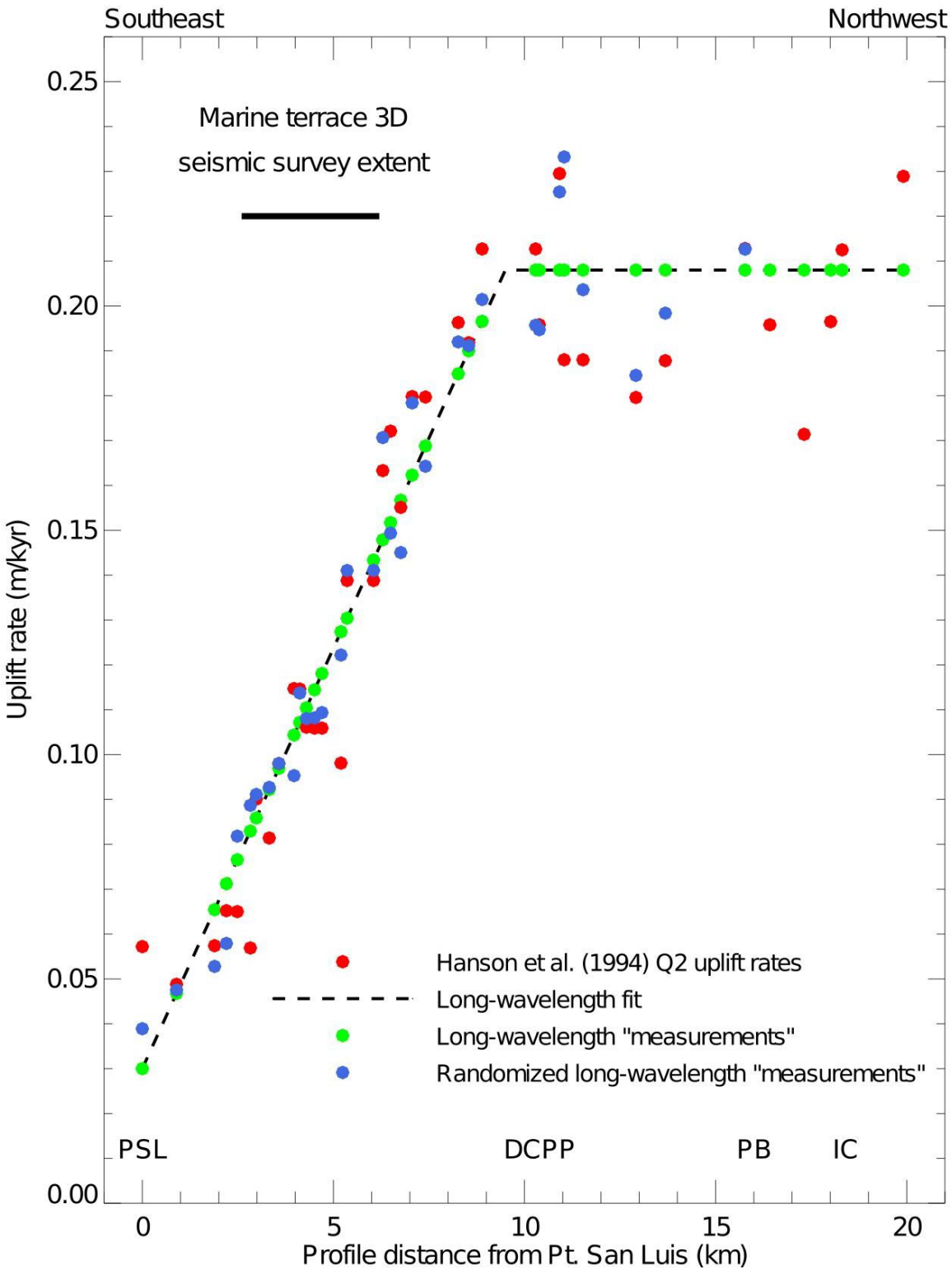

Figure S8. Simulation 2 of Hanson et al. (1994) uplift rate data with red circles as the measured uplift rates from Hanson et al. (1994).

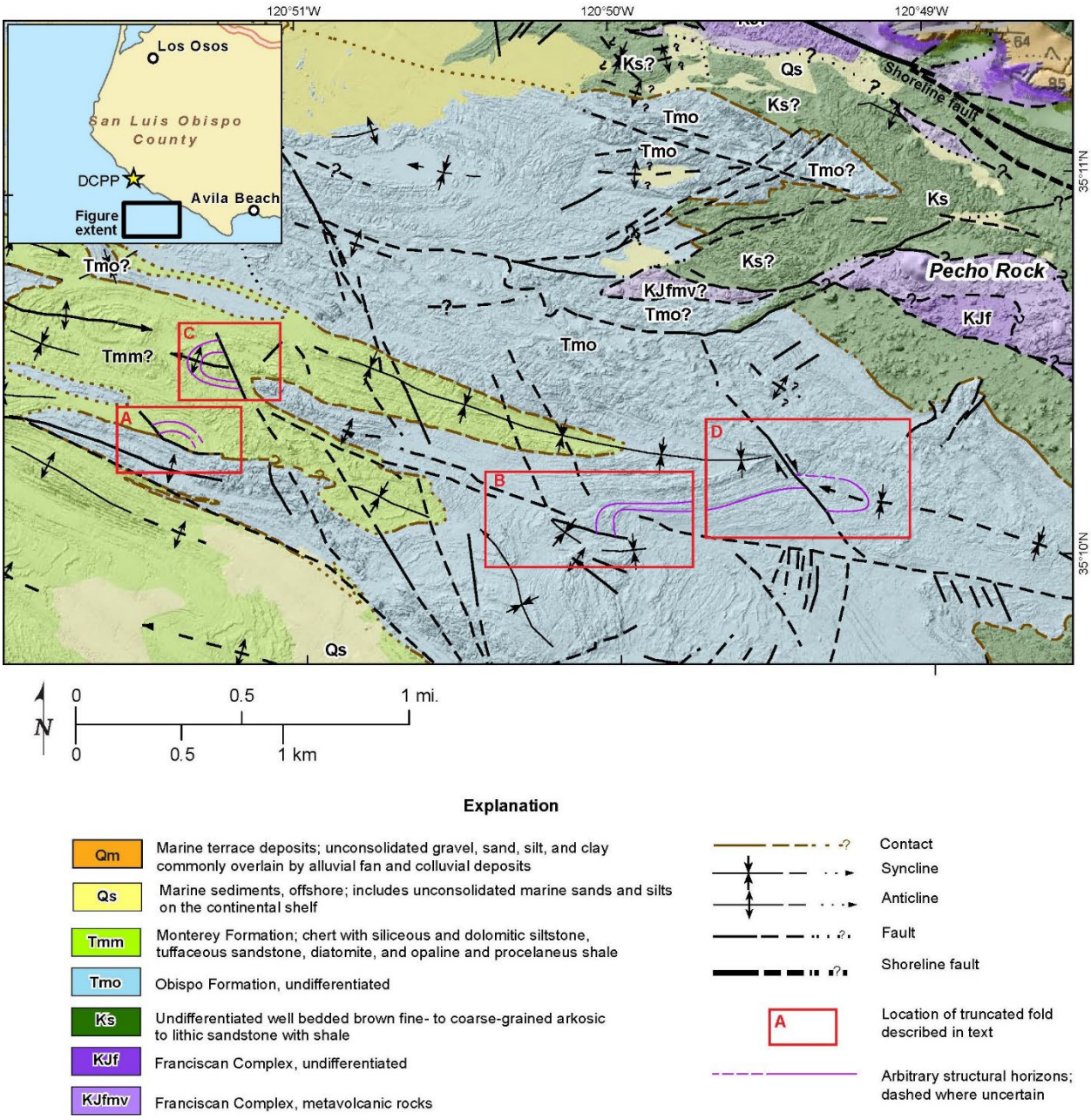

Figure S9. Seafloor roughness-shaded geologic map showing folds truncated by strike-slip faults east of the HFZ. An early Quaternary compressional phase of deformation is characterized by thrust faulting, flexural slip folding, and short-wavelength anticline-syncline pairs formed during basin inversion and formation of the positive-topography Pismo synclinorium. Later (120 ka to modern) deformation is characterized by both vertical strike-slip faulting and regional uplift, with no significant vertical offset of the emergent Q2 marine terrace platform from Islay Creek to Pt. San Luis.

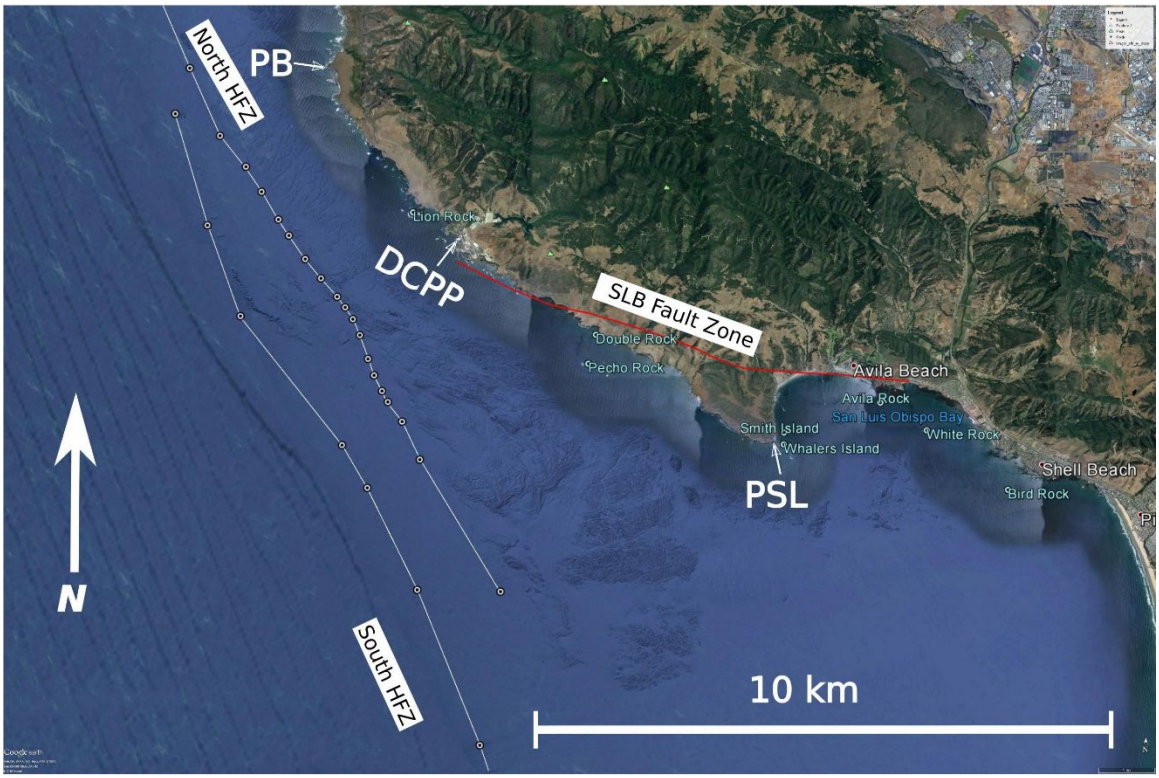

Figure S10. Location of the San Luis Bay fault zone (red line) relative to the HFZ (white lines with black-white circles showing control points. Specific geographic locations referred to in the main text are Point San Luis (PSL), Point Buchon (BP), and the Diablo Canyon Power Plant (DCPP).

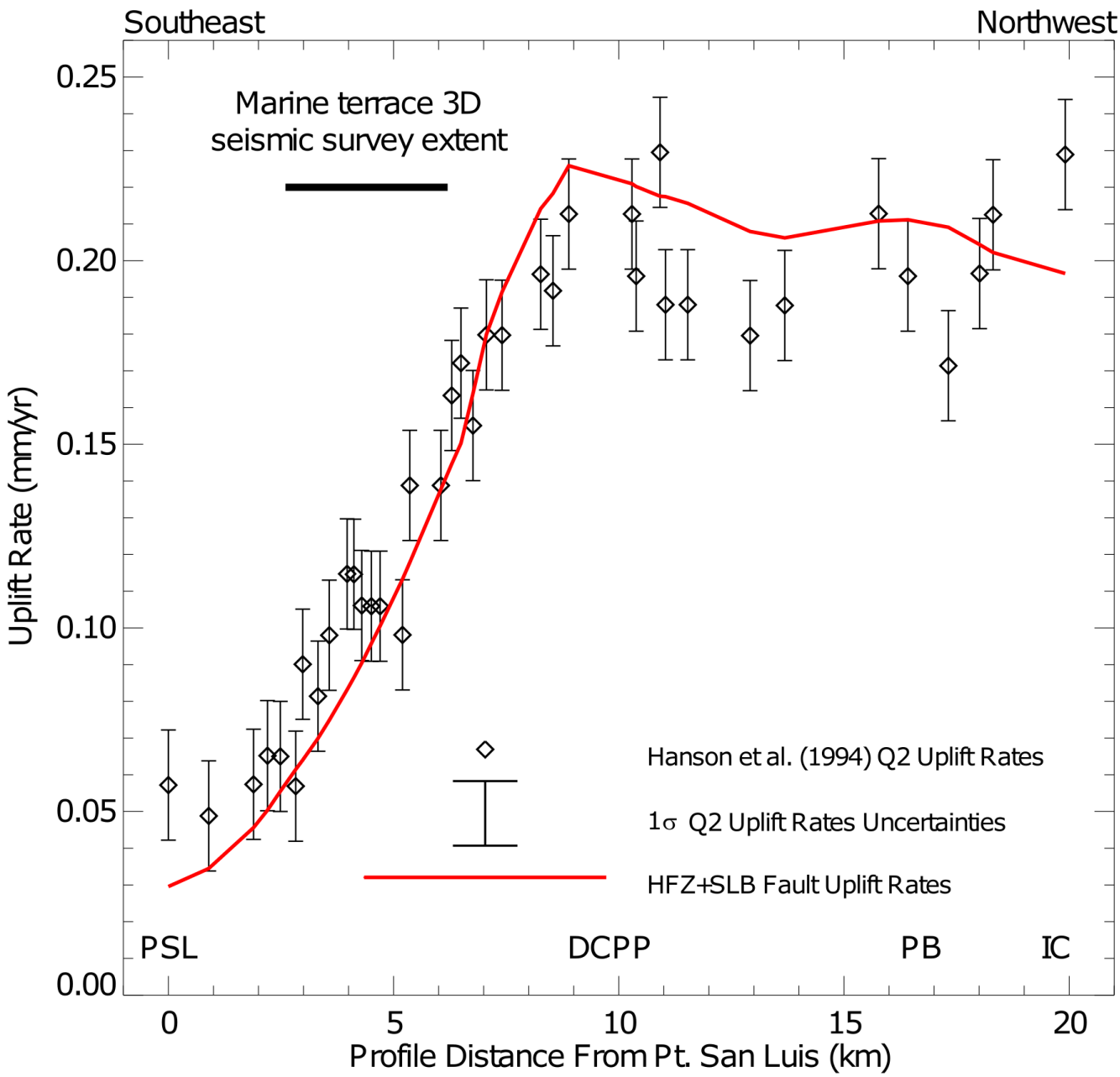

Figure S11. Comparison of observed (diamonds) and calculated uplift rates (red line) with 1σ uplift rate measurement uncertainties as the uncertainty bars. Calculated uplift rates include deformation from the final HFZ slip rate model and a 0.04 m/kyr reverse slip rate on the SLB fault. The calculated uplift rates are slightly incompatible with the observed uplift rates with four calculated uplift rates deviating from the measured uplift rates by more than 2σ; on average two incompatible calculated uplift rates are consistent with a sample size of 38 observations.